Droplet evaporation-based approach for microliter fuel property measurements

Wanjun Dang[1*], Mohana Gurunadhan[1†], William Ard[1†], Ingmar Schoegl[1†] and Shyam Menon[1†]

[1]Mechanical and Industrial Engineering Department, Louisiana State University, 3261, Patrick F Taylor Hall, Baton Rouge, 70803, LA, USA.

*Corresponding author(s). E-mail(s): wdang3@lsu.edu;
Contributing authors: mgurun1@lsu.edu; ward2@lsu.edu; ischoegl@lsu.edu; smenon@lsu.edu;
†These authors contributed equally to this work.

Abstract

Small-volume, high-throughput screening techniques are sought to enable downselection from a large candidate pool of bio-blendstocks to a select few, having physical properties consistent with requirements of downsized, turbo-boosted internal combustion engines. This work presents a droplet evaporation-based approach to predict heat of vaporization, vapor pressure, diffusion coefficient, and Lennard-Jones parameters for an unknown fuel. Two different schemes, considering the isothermal evaporation of a moving droplet in ambient air are proposed, which combine droplet velocity and temperature measurements, with some known properties to predict unknown properties. The schemes utilize an inverse solution of a transient model of droplet evaporation solved in an iterative fashion. The baseline scheme is evaluated using evaporation measurements of three liquid fuels in a temperature-controlled chamber, yielding temperature-dependent heat of vaporization and vapor pressure predictions within 10%, and 20% respectively of reference values. Incorporation of droplet temperature through the advanced scheme is found to significantly improve prediction quality, with deviations less than 2% and 1% for heat of vaporization and vapor pressure,

while also predicting diffusion coefficient and Lennard-Jones parameters within 5% and 8% respectively. The combined set of approaches, primarily tracking a droplet evaporation process can be incorporated into a small-volume, high-throughput fuel screening process.

Keywords: Droplet evaporation, Heat of vaporization, Vapor pressure, Abramzon-Sirignano model, Diffusion coefficient, Lennard-Jones parameters

1 Introduction

Fuel spray plays a key role in the overall performance and emissions of direct-injected, liquid hydrocarbon-fueled, internal combustion (IC) engines. The injection process and resulting spray introduces fuel into the engine cylinder. Subsequent spray breakup, atomization, evaporation, and fuel-air mixing critically impact the ensuing ignition and combustion processes. Fuel physical properties have a direct impact on the above-mentioned in-cylinder processes particularly those preceding ignition and combustion. Spray breakup through atomization, and its penetration into the cylinder volume are impacted by fuel surface tension and viscosity [37]. Once atomized into a distribution of finely-sized droplets, evaporation and fuel-air mixing processes are directly coupled to the heat of vaporization and vapor pressure of the fuel, as dictated by the ambient conditions surrounding the fuel droplets [27]. Heat of vaporization (HOV) or latent heat is the energy required for phase change of the liquid fuel. Vapor pressure is a measure of the pressure exerted by the fuel vapor in thermodynamic equilibrium condition with its liquid phase. Heat of vaporization and vapor pressure (P_{vap}) can be related to each other through the Clausius-Clapeyron equation,

$$ln(P/P_0) = -HOV/(RT) + C \tag{1}$$

where P is the vapor pressure at the corresponding temperature, T, R is the gas constant, P_0 is the reference pressure and C is the intercept of the linear fit from plotting the natural log of vapor pressure against temperature.

The impact of HOV is primarily through in-cylinder thermodynamics as affected by the fuel droplet evaporation processes leading to the formation of the fuel-air mixture. The energy required for evaporation is provided by the ambient air surrounding the droplets in the engine cylinder. In the process, as fuel evaporates, it results in cooling of the in-cylinder charge. This reduction in charge temperature, and corresponding increase in intake air density results in improved volumetric efficiency of gasoline engines, particularly at part load conditions [34]. Evaporative cooling as affected by fuel HOV also has a significant effect on knock suppression in direct-injected (DI) gasoline engines. Previous studies conducted on downsized, turbo-boosted engines have shown that evaporative cooling provides an effect comparable to increasing the octane rating of the fuel by about 5 units [4], allowing an increase in compression ratio by about 1 unit [26]. Knock resistance of a fuel is commonly expressed through the octane index (OI) [16], expressed as,

$$OI = RON - K \cdot S \tag{2}$$

where RON is the Research Octane Number and S is the octane sensitivity ($RON - MON$), with MON being the Motor Octane Number. K is an engine constant that depends on pressure-temperature history of the unburned charge in the engine cylinder and typically has negative values at the most knock-limited operating conditions. While K is not a fuel property, the end-gas pressure-temperature history which K relates to, is affected by fuel composition and properties including HOV. Higher HOV reduces charge temperature,

leading to more negative values of K, and thus improves fuel anti-knock properties. This is directly evidenced by numerous studies considering the impact of ethanol and other alcohol blends on engine knock [26, 5, 32, 9].

Vapor pressure is another important physicochemical property, widely used in assessing the quality of gasoline along with other quantities such as distillation parameters, specific gravity, octane number, and octane index. Vapor pressure is directly related to the volatility of the fuel and has a direct influence on engine performance as well as fuel production and transportation logistics. Fuel vapor pressure is required to meet specific standards to ensure safety considerations in the transport and storage of fuels to avoid accidents and minimize losses through evaporation. Fuels with lower vapor pressure are harder to vaporize resulting in poor combustion efficiency [22]. On the other hand, fuels with high vapor pressure can generate volatile organic compounds leading to uncontrolled air-fuel ratio affecting the combustion process. These considerations have made it a requirement to maintain fuel vapor pressure within an acceptable range.

Given their significant influence on fuel transportation, storage, and evaporation and combustion characteristics impacting engine performance, standard testing approaches and procedures have been established for measuring HOV and vapor pressure. A differential scanning calorimeter (DSC)/thermogravimetric analysis (TGA) is a standard tool used in HOV measurement of fuels and blends. A Q600-series model from TA instruments used in previous studies [8] utilizes sample sizes ranging from 40–100 μl and calculates HOV on the basis of heat energy required for sample evaporation. Gasoline volatility is typically expressed through the Reid Vapor Pressure (RVP). RVP represents the fuel industry standard for vapor pressure and is the value measured at 37.8°C in a container with a vapor to liquid ratio (V/L)

of 4:1 [20]. RVP can be measured through a variety of Reid methods including ASTM D-323 and D-4953, which are referred to as the original and dry Reid methods, as well as D-5191 and D-5482 which are referred to as miniaturized methods [14, 17, 12]. Sample sizes range from 100 cc for the original and dry Reid methods to between 1–10 cc for the miniaturized methods. ASTM D-6378 is yet another measurement procedure requiring 5–15 cc particularly addressing limitations of previous methods for dealing with volatile fuel components. All of the above mentioned RVP measurement methods except D-323 are capable of operation with oxygenated fuels which is relevant to this work.

As technologies advance to improve SI engine efficiency through strategies such as direct injection, higher compression ratios, turbocharging, and downsizing [5], fuel sprays are subject to considerably different in-cylinder operating conditions. Characterizing fuel physical properties at these conditions is essential to understanding spray behavior and mixture preparation prior to ignition. While standard techniques of HOV and vapor pressure measurement as described previously operate with fuel samples of $\mathcal{O}(ml)$, this study is motivated by a desire to develop screening approaches compatible with fuel samples of $\mathcal{O}(\mu l)$ capable of high throughput. This will enable rapid screening approaches to downselect from a large number of candidate fuels that can be narrowed down to a fewer number based on threshold requirements for physical properties such as viscosity, surface tension, HOV, and vapor pressure. Development of rapid screening tools is one of the objectives of ongoing work through the DOE's (Department of Energy) Co-Optima initiative. This initiative aims to identify potential gasoline blendstocks with viable biomass-derived production pathways to incorporate renewable domestic biomass into the gasoline supply chain [21]. Previous work by the authors focused on small-volume, high-throughput approaches for surface tension and viscosity

measurement [6, 7]. This work pursues similar objectives with respect to determining HOV and vapor pressure for liquid fuels. As the prediction methods developed in this work evolved, it was realized that the overall approach could be extended for prediction of additional physical properties including diffusion coefficient and Lennard-Jones (LJ) parameters, which play a significant role in modeling transport processes of fuel vapor for numerical simulations of in-cylinder engine processes.

The paper is laid out as follows. The approach used in this work that leverages droplet evaporation processes as modeled by a zero-dimensional transient simulation that captures droplet size change for stationary and moving liquid fuel droplets is discussed. Two different schemes as made feasible using experimental data and the 0D simulation are discussed along with the inputs required for each and their respective outputs. The experimental setup and procedure used to measure fuel droplet evaporation rate at controlled temperature conditions is presented and discussed. Results obtained from a baseline scheme requiring only droplet size change measurements are presented for HOV and vapor pressure predictions. Tested fuels include a pure component, a gasoline surrogate, and a bio-blendstock. Next, results are presented for HOV, vapor pressure, diffusion coefficient, and LJ parameters as can be obtained from a more advanced scheme requiring additional inputs including droplet velocity and temperature. Results are discussed and finally conclusions are presented.

2 Approach

As described in the introduction, this work is motivated by development of techniques for HOV and vapor pressure measurement of liquid hydrocarbon fuels, suitable for use in high-throughput, rapid-screening approaches for bio-derived gasoline blendstocks. In previous related efforts [6, 7], a droplet

oscillation-based approach to measure surface tension and viscosity of fuels at ambient and elevated temperatures has been presented. In these studies, droplets were generated using a piezoelectric droplet generator capable of operating with μl samples. In an effort to constrain the sample volume requirement, the approach proposed in this work utilizes the same droplet generation hardware. Droplet oscillation, which begins at the point of droplet generation and ends a short while after, can be used to measure surface tension and viscosity. The proposed approach intends to use evaporation processes of the droplet post oscillation, to measure HOV and vapor pressure. This provides a streamlined approach utilizing the minimum quantity of the fuel sample. Besides being capable of making measurements with small sample sizes, the timescale of the entire process from the point of droplet jetting to complete evaporation is small ($\mathcal{O}(ms)$), thus ensuring compatibility for a rapid screening approach. Finally, with minor modifications and packaging, it is possible to integrate the physical property evaluation techniques based on droplet oscillation and evaporation with chemical kinetic property evaluation techniques being developed using a micro-combustor setup [15].

A liquid fuel droplet subjected to a controlled temperature environment undergoes evaporation under stationary or moving conditions. The evaporation process for small droplets involving heat and mass transfer is controlled primarily by the ambient conditions and liquid properties including HOV and to a smaller degree by second-order effects such as circulation within the droplet and water condensation on the droplet surface. A large body of work has been carried out to model droplet evaporation processes incorporating various levels of complexity, which are detailed in a number of review publications [1, 2, 31]. The approach used in this work is to use an appropriate droplet evaporation

model to calculate fuel properties of interest including HOV and vapor pressure, using measurements obtained from experiments with moving, evaporating droplets. Measurements can include various parameters including droplet size, velocity, and temperature as will be discussed in further detail later in this section. The approach is illustrated schematically in Fig. 1. A similar approach

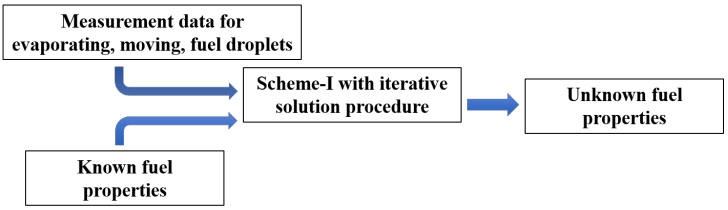

Fig. 1 Fuel property prediction approach using droplet evaporation measurements.

was followed by Ray [28] who used observations of size change of evaporating droplets at stationary conditions as obtained through droplet levitation, to estimate ultra-low vapor pressures of fluids used in aerosol research. Ray used a Maximum Likelihood Estimation (MLE) approach to determine fluid physical properties including HOV and vapor pressure as well as molecular dynamic parameters such as the parameters relating to the Lennard-Jones potential. This approach differs from Ray's work in that the focus is on using moving droplets to allow a simpler experimental setup without the need to levitate droplets in a constant temperature chamber. This work utilizes the Abramzon and Sirignano (AS) model [1] to simulate the evaporation process of moving droplets. The Abramzon model incorporates Stefan flow and effects of convective heat and mass transfer using a "film theory", which in essence introduces a vapor-gas film between the droplet surface and ambient atmosphere, effectively providing resistance to heat and mass exchange as shown schematically in Fig. 2. Model assumptions include quasi-steady heat and mass transfer, temperature dependent thermo-physical properties, uniform temperature and fuel

vapor concentration on the droplet surface, spatially-uniform but time-varying droplet temperature, and no velocity field within the droplet.

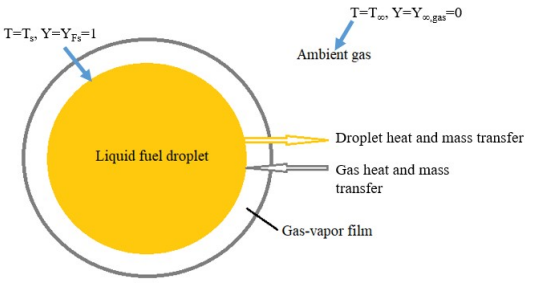

Fig. 2 Droplet evaporation model incorporating the liquid-vapor film.

Source terms considered in the model include those for:

- Droplet velocity:

$$\frac{du}{dt} = -\frac{3C_D\bar{\rho_f}}{8D_l\rho_l}(u-u_\infty)^2 + g_0\left(1-\frac{\bar{\rho_f}}{\rho_l}\right) \tag{3}$$

  where $\bar{\rho}_f$ is the density of the vapor in the film, g_0 is the acceleration due to gravity, C_D is the drag coefficient, u is the droplet velocity, u_∞ is the ambient gas velocity, D_l is the droplet diameter and ρ_l is the liquid density.

- Droplet diameter:

$$\frac{dD_l}{dt} = -\frac{2\dot{m}_l}{\pi\rho_l D_l^2} \tag{4}$$

  where $\dot{m}_l$ is the net instantaneous evaporation rate of the droplet in kg/s.

- Droplet temperature:

$$\frac{dT_l}{dt} = \frac{\dot{Q}_l}{m_l C_{pl}} \tag{5}$$

  where $\dot{Q}_l$ is the rate of heat transfer to the liquid droplet and m_l is the mass of the droplet.

In the above transient governing equations, C_D, $\dot{m}_l$ and $\dot{Q}_l$ are defined based on the operating conditions and properties of the fuel and carrier gas. From the mass and energy balance equations at the interface, evaporation rate, $\dot{m}_l$ is defined as:

$$\dot{m}_l = \pi \bar{\rho}_f \bar{\chi}_{fc} D_l \mathrm{Sh}^* \ln(1 + B_M) = \pi \frac{\bar{k}_f}{\bar{C}_{pF}} D_l \mathrm{Nu}^* \ln(1 + B_T) \tag{6}$$

where,

$$B_M = \frac{(Y_{Fi} - Y_{F\infty})}{(1 - Y_{F\infty})}, \qquad B_T = \frac{\bar{C}_{pF}(T_\infty - T_i)}{H_F(T_i) + \frac{\dot{Q}_l}{\dot{m}_l}} \tag{7}$$

In the above equations, $\bar{\chi}_{fc}$ is the diffusivity in the film, B_M refers to the mass transfer number, calculated from fuel vapor mass fraction at the droplet interface (Y_{Fi})and in the far field ambient ($Y_{F\infty} = 0$) and B_T refers to the heat transfer number, defined using the droplet interface temperature T_i, far field ambient temperature T_∞, heat of vaporization of the fuel H_F evaluated at droplet temperature T_i and the average specific heat of fuel vapor in film ($\bar{C}_{pF}$) evaluated at film temperature $\bar{T}_f$. Nu^* and Sh^* are the modified Nusselt number and Sherwood number, respectively, for a spherical droplet, considering the effect of blowing. The definition of Nusselt number, Sherwood number and film temperature, based on the work of Abramzon et al. [1], is provided in Appendix A. Nu^* is a function of Reynolds number (Re) and Prandtl number (Pr), while Sh^* is a function of Re and Schmidt number (Sc). For the droplet diameter and velocity scales considered in the present work, Re is found to be <0.1 and the effect of velocity through Re on property predictions can be neglected. However,this effect should be considered for larger droplets with higher velocities. The subscript f refers to the gas phase properties in the gas-vapor film, l refers to the liquid properties, i indicates the properties at the liquid surface (liquid-gas interface) and the fuel vapor properties are indicated by subscript F. The interface temperature, $T_i = T_l$, considering infinite

thermal conductivity for the droplet, which disregards spatial temperature gradients in the droplet.

The net heat transfer rate $\dot{Q}_l$ can be evaluated using the combined equations of heat transfer number (Eq. 7) and interfacial energy balance (Eq. 6). In the transient equation for droplet velocity (Eq. 3), drag coefficient C_D is based on the correlation for 'standard drag curve' provided in the work of Putnam et. al [24] , defined as:

$$C_D = \frac{24}{\mathrm{Re}} \left\{ 1 + \frac{\mathrm{Re}^{2/3}}{6} \right\} \tag{8}$$

where Re is the Reynolds number, defined as $\frac{\bar{\rho}_f D_l |u - u_\infty|}{\bar{\mu}_f}$. All the gas properties in the film are defined as a function of average fuel vapor mass fraction $\bar{Y}_f$, in the film and average temperature of the film ($\bar{T}_f$). The equations used for film properties, used in the current work, are detailed in Appendix A.

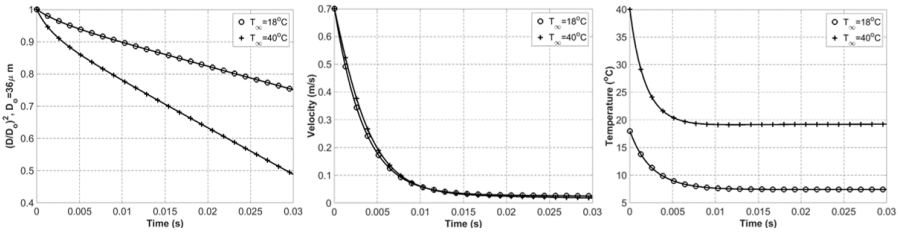

Fig. 3 Predictions for droplet evaporation using the AS model for PRF-84 at two different ambient temperatures showing variation of the square of the droplet diameter, droplet velocity, and droplet temperature as a function of time.

In the conventional AS method, the governing equations given by Equations 3, 4, 5, and 6 are solved using an explicit transient solver, with fuel transport properties and initial conditions as the input. It is noticed, based on the simulation of fuel droplets of research interest, that after the initial transients, droplet temperature (T_i) and velocity reach a quasi-steady-state and the square of droplet diameter (D_l^2) exhibits a quasi-linear behavior (constant slope) with time. This is illustrated by simulation results shown in Figure 3

where the evaporation process of a droplet of PRF-84 was modeled using the AS model for two different ambient air temperatures. In the present work, it is desired to implement an inverse AS algorithm, wherein, measurement data from observations of droplet evaporation at controlled conditions will be used as inputs to estimate unknown fuel physical properties. In pursuing this approach, it is realized that the logic described above can be implemented in different ways depending on which quantities are measured in the experiments. Further, in addition to the measured quantities, some physical properties for the unknown fuel are required as inputs to the algorithm. These details are summarized in Table 1. The table provides details of the required measurement and physical property inputs along with the numerical predictions that can be made utilizing the inverse AS algorithm. Note that properties mentioned in the table pertain to the values for the fuel vapor. Further, numerical predictions obtained for fuel physical properties correspond to those at a steady state temperature (T_i), as reached by the droplet during the evaporation measurements in the experiment.

Table 1 summarizes two different schemes which utilize measurements along with input data for known physical properties to give numerical predictions for unknown physical properties. As the number of measured quantities increases from Scheme-I to Scheme-II, the required number of known physical properties to be used as inputs to the algorithm decreases. Numerical predictions listed for each Scheme represents temperature-dependent values that can be obtained from the calculations except for Lennard Jones parameters which are temperature-independent. In the present work, the major focus is on predictions of temperature-dependent HOV and vapor pressure. Accordingly, the viability of Scheme-1 as summarized in Table 1 is now demonstrated

Table 1 Summary of required inputs and predicted outputs using Scheme-I and Scheme-II.

	Input Data		**Numerical predictions**
	Measurements	**Properties**	
Scheme-I	♦ D_l, $\frac{dD_l^2}{dt}$	• Density (Liquid, vapor) • Viscosity • Thermal conductivity • Specific heat • Diffusion coefficient • Boiling point	✓ Vapor pressure, P_{vap} ✓ Heat of vaporization, H_F
Scheme-II	♦ D_l, $\frac{dD_l^2}{dt}$ ♦ u, $\frac{du}{dt}$ ♦ T_i	• Density (Liquid, vapor) • Viscosity • Thermal conductivity	✓ Vapor pressure, P_{vap} ✓ Heat of vaporization, H_F ✓ Diffusion coefficients ✓ Lennard Jones, (σ, ϵ) ✓ Boiling point, (T_{boil})

using experimental measurements and the inverse droplet evaporation model approach.

Details of Scheme-I are summarized in Table 1 and shown as a flowchart in Fig. 4. Droplet diameter and the quasi-linear slope of change in square of droplet diameter (D_l^2) with time, are provided by the experiment. Fuel vapor properties are evaluated using empirical/analytical equations described in Appendix A. Using these inputs, droplet temperature (T_i), temperature-specific vapor pressure (P_{vap}) and heat of vaporization (H_F) can be evaluated using an iterative approach. The pertinent steps of the Scheme-I algorithm are as listed below:

1. To start the algorithm, the initial droplet temperature is assumed to be equal to far field ambient temperature ($T_i = T_\infty$). This temperature will be corrected in an iterative manner.

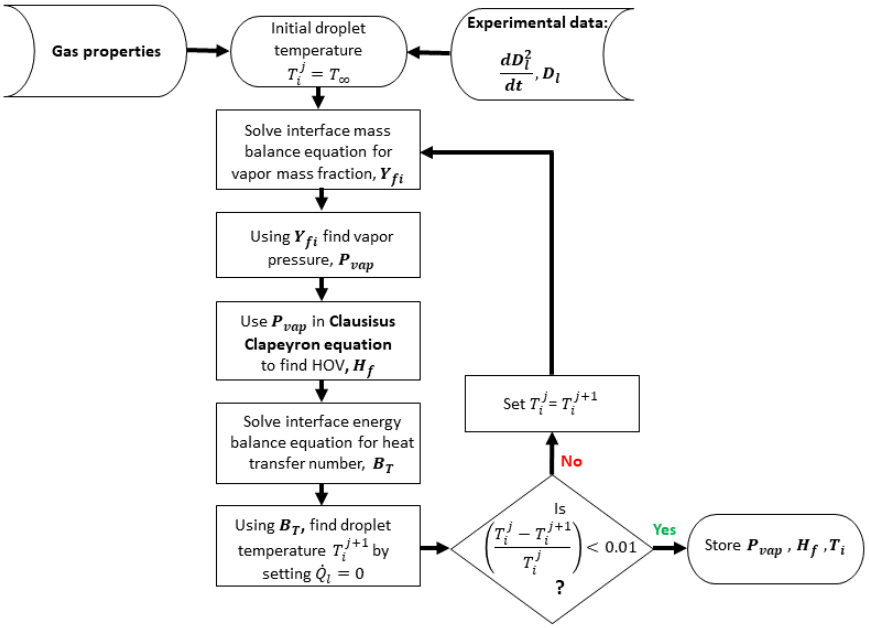

Fig. 4 Approach used in HOV and vapor pressure estimation using measurements and the droplet evaporation model as implemented through Scheme-I.

2. Using the droplet temperature (T_i), and experimental data and property inputs as listed in Table 1, the interfacial mass balance equation is solved for fuel vapor mass fraction at the droplet interface. Accordingly, Eq. 6 can be rewritten as an implicit function of droplet temperature and interface fuel mass fraction.

$$\dot{m} - \pi \bar{\rho}_f \bar{\chi}_{fc} D_l \mathrm{Sh}^* ln(1 + B_M) = F(Y_{Fi}, T_i) = 0 \tag{9}$$

The above equation can be solved for unknown interface mass fraction Y_{Fi}, using any standard root finding technique. It is to be noted that the mass flow rate ($\dot{m}$) and droplet diameter (D_l) used in Eq. 9 correspond to values after a steady-state droplet temperature is achieved.

3. The interface mass fraction (Y_{Fi}) is utilized to find the instantaneous vapor pressure of the droplet, which is defined as

$$P_{vap} = P_{\infty} \left\{ \frac{Y_{Fi} MW_c}{MW_F + Y_{Fi}(MW_c - MW_F)} \right\} \tag{10}$$

where MW is the molecular weight of carrier gas (subscript 'c') and fuel (subscript 'f').

4. With vapor pressure P_{vap} as the input, Heat of vaporization is evaluated using the Clausius- Clapeyron equation, as shown below:

$$H_F = -\ln\left(\frac{P_{vap}}{P_{\infty}}\right) \frac{R_u}{MW_F \left[\frac{1}{T_i} - \frac{1}{T_{boil}}\right]} \tag{11}$$

where T_{boil} is the fuel boiling point at the ambient pressure during the experiment.

5. The interface mass fraction is further utilized to evaluate the heat transfer number B_T. Similar to step 2, the interfacial energy balance equation, Eq. 6, can be rewritten as an implicit function of B_T, T_i and Y_{Fi}, given by:

$$\dot{m} - \pi \frac{\bar{k}_f}{\bar{C}_{pF}} D_l \mathrm{Nu}^* ln(1 + B_T) = G(Y_{Fi}, T_i, B_T) = 0 \tag{12}$$

The above equation is solved for unknown heat transfer number B_T, using any standard root finding technique.

6. As observed from simulations using the AS model, the fuel droplet reaches a quasi-steady temperature, after the initial transients, which implies that the net heat transfer rate, $\dot{Q}_l = 0$. Using this observation, the equation for heat transfer number B_T (Eq. 7), is modified for the unknown droplet temperature T_i.

$$T_i = \frac{-B_T H_F}{\bar{C}_{pF}} + T_{\infty} \tag{13}$$

7. The droplet temperature is updated using the above value and the Steps 1 to 6 are repeated until the change in temperature, from the previous

iteration, is negligible (until convergence). In the numerical trials conducted, convergence was observed in less than 15 iterations.

The algorithm Scheme-I is now used with evaporation measurements for various fuels of interest to demonstrate the validity of the approach. A detailed listing of steps to accomplish Scheme-II as summarized in Table 1 is provided in Appendix A.

3 Experiment

3.1 Experimental setup

The experimental setup for droplet evaporation is shown schematically in Figure 5. A piezoelectric droplet generator (Microfab PH-41, 30μm nozzle) is placed inside a closed, cylindrical metal chamber, and used to inject a continuous stream of droplets into the chamber. A PID controller (Extech 48VFL) along with a heating element wrapped around the chamber are used to control the chamber temperature. Fuel is supplied to the droplet generator from a reservoir kept outside the chamber at room temperature(22°C). A signal generator (Microfab JetDrive V (CT-M5-01)) provides pulses to actuate the droplet generator. The piezoelectric element on the actuator expands or contracts according to the polarity of the signal. Droplets are formed at the nozzle tip as a result of the fast deformation of the piezoelectric material. A pressure controller (MicroFab CT-PT-21) is used to select positive or negative back pressure to sustain a balancing force on the fluid column at the exit plane of the nozzle. The back pressure is provided by a compressed air source and a vacuum pump (Koge electronic, KPV20A-6A), which respectively provide positive and negative back pressures to the pressure controller.

The frequency of the waveform pulse controls the droplet spacing. A machine vision camera (Sentech STC-MB33USB) mounted on a vertical traverse is used to obtain a live video of the droplet trail within the chamber. Images are extracted from the video for processing. The camera has optical access into the chamber through the quartz windows located on either side of the pressure chamber. The camera has a resolution of 4.56 μm/pixel using a Precise Eye lens and adapter. The light source for the camera is comprised of four LED's (Broadcom HLMP- CM1A-560DD), which are soldered on a circuit board located inside the chamber and provided with constant voltage using an external power supply (BK Precision Model 1621A).

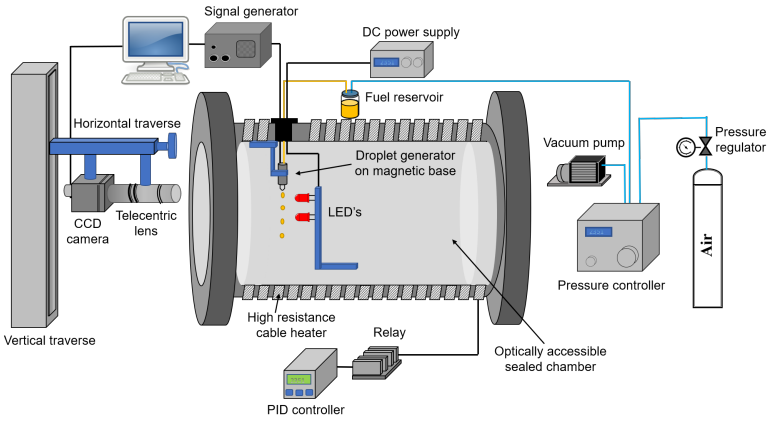

Fig. 5 Droplet evaporation experimental setup.

3.2 Measurement procedure

To conduct the tests, the chamber doors are closed and air is cycled through the chamber to remove any remnant fuel vapor from previous tests. All tests were conducted at atmospheric pressure. Next, the temperature controller is set to the desired set-point for chamber temperature. Chamber temperature is monitored at different locations until they reach steady state values. This

typically takes about 30-40 minutes. Once the desired temperature is reached inside the chamber, the back pressure controller is used to purge some of the fuel thereby producing a well-defined liquid meniscus which can be seen from the camera interface to a computer. Next, using the back pressure controller, the meniscus is carefully aligned with the exit plane of the glass nozzle. Once aligned, the desired waveform pulse is applied to produce the liquid droplet train with the required frequency. The camera is used to take a live video of the droplet trail at various downstream locations from the nozzle by moving it using the vertical traverse. Distance measurements are facilitated by an image calibration that provide a pixel to micron conversion. Using the calibration, droplet size and location from the nozzle exit are determined.

3.3 Image processing

Image processing and analysis to capture the droplet edge and estimate droplet diameter was carried out using a custom Matlab package. The process includes background subtraction, batch cropping, anisotropic filtering, and edge detection by a subpixel method to capture the droplet shape. A detailed description of these steps can be found in previous work [6].

3.4 Fuels tested

Fuels of interest to this work comprise of pure components and blends which have been researched as part of the DOE Co-Optima program to develop bio-blendstocks for use in advanced internal combustion (IC) engines. While this includes a large number of pure components and blends, the current work focuses on a subset of these as listed in Table 2. PRF-84 represents a two-component blend containing 84% *iso*-octane (Acros Organics, 99.5%) and 16% *n*-heptane (Acros Organics, 99.5%) by volume. *n*-heptane has a Cetane number similar to that of commercial diesel fuel and has been used as a diesel

surrogate in studies of advanced combustion strategies including Homogeneous Charge Compression Ignition (HCCI) [10] and Reactivity Controlled Compression Ignition (RCCI) [25]. PRF-84 on the other hand represents a simple two-component gasoline surrogate used in studies on conventional Spark Ignition IC engines [30]. Isobutanol has been identified by DOE's Co-Optima program as being one of the top ten bio-blendstocks for turbocharged gasoline engines [13] and is seen as a potential second generation biofuel that can be viably sourced from biomass [3].

Table 2 lists reference values for various fuel physical properties including RVP and vapor pressure measured at 100°F (37.8°C). It is seen that while RVP measurement requires evaluating vapor pressure at 100°F and a vapor/liquid ratio of 4:1, a rough estimate of RVP can be obtained simply by considering the fuel vapor pressure at 100°F. This approach is assumed to be acceptable for the purposes of fuel screening, which forms the ultimate goal of the methods proposed in this work to evaluate fuel physical properties.

Name	**Functional group**	**Formula**	**Boiling Point**	**RVP**	**Vapor pressure @ 100°F**	**HOV @ 25°C**
n-heptane	Alkane	C_7H_{16}	98.4	12.4	11.1	364.8
Isobutanol	Alcohol	$C_4H_{10}O$	108	3.3	3.3	692.5
PRF-84	Blend	16% C_7H_{16}, 84%C_8H_{18}	98.7	N/A	11.6	319.8
			$^\circ C$	kPa	kPa	kJ/kg

Table 2 Properties of fuels tested in this work as relevant for use in advanced SI engines [35, 23].

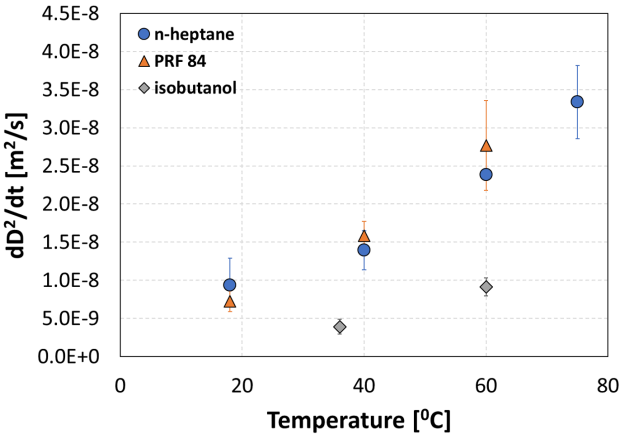

Fig. 6 Evaporation rate as expressed by the rate of change for diameter-squared as a function of ambient air temperature for the fuels tested in this work.

4 Results and discussion

4.1 Measurements

Figure 6 shows the evaporation rate expressed as dD^2/dt as a function of ambient temperature for the three different fuels tested in this study. As can be observed, dD^2/dt increases with temperature for all fuels as expected. Further, dD^2/dt for *n*-heptane closely tracks that of PRF 84 given that the second component making up PRF 84 (*iso*-octane) has a volatility very similar to that of *n*-heptane. On the other hand isobutanol has a lower vapor pressure (Table 2) resulting in a lower evaporation rate for the same ambient temperature. Figure 6 also shows uncertainty estimates in the form of individual error bars for each data point. The uncertainty values represent fluctuations when evaporation rate measurements are repeated for a given fuel at a certain ambient temperature condition. They are estimated using a Student's t-distribution as appropriate for a small sample size for a confidence interval of 95%. They result from uncertainty induced by the resolution of the imaging setup and subsequent edge detection techniques. The measured evaporation rate can be

compared with a predicted value based on calculations using the AS model at identical conditions. Figure 7 shows the difference between measured and predicted values as a function of temperature. As observed in Fig. 7, the % deviation decreases for all cases with increase in temperature. This is attributed primarily to increasing change in droplet size over the course of the observation period due to higher evaporation rates resulting in lower sensitivity to error sources.

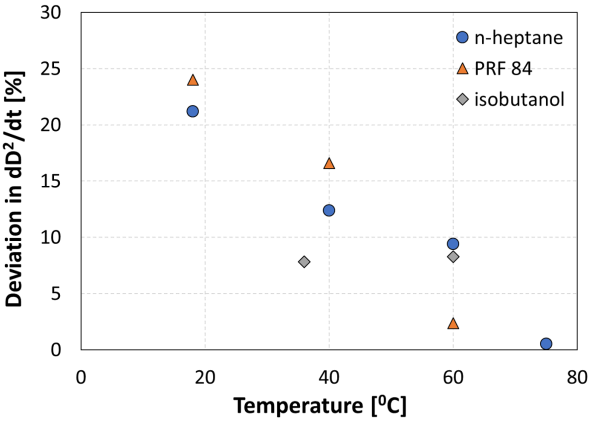

Fig. 7 Deviation in measured evaporation rate from value predicted by the droplet evaporation model as a function of ambient air temperature.

4.2 Physical property predictions using Scheme I

Table 3 shows the results obtained from Scheme-I calculations using experimental measurements reported in Fig. 6. Predicted values for temperature-dependent HOV and vapor pressure for the three fuels tested in this work are presented along with reference values obtained from literature. It should be noted that data presented in Table 3 and further plotted in Fig. 8 are results averaged over multiple experimental data sets. Table 3 includes uncertainties calculated using Student's t-distribution as discussed earlier. Deviation

Fuel	**Temperature**	**HOV**			**Vapor pressure**		
		Predicted	Reference	Deviation	Predicted	Reference	Deviation
n-heptane	18	340 ± 50	374	9.1	2.78 ± 0.9	2.41	15.4
	40	390 ± 40	367	6.4	3.86 ± 0.7	4.6	16
	60	370 ± 10	363	2.1	6.51 ± 0.1	6.84	4.9
	75	364 ± 40	360	1.1	8.44 ± 1.2	8.71	3.1
PRF 84	18	343 ± 20	328	4.7	2.04 ± 0.4	2.60	21.7
	40	339 ± 20	323	5.3	4.13 ± 0.5	4.88	15.3
	60	325 ± 50	318	2.2	6.83 ± 1.4	7.34	6.9
isobutanol	36	676 ±60	690	2.0	1.39 ± 0.3	1.44	3.0
	60	673 ± 50	674	0.1	3.02 ± 0.4	3.18	5.0
	°C	kJ/kg		%	kPa		%

Table 3 Results from calculations using Scheme I.

reported in Table 3 is computed as the difference between predicted and reference values.

Figure 8 shows predicted HOV and vapor pressure plotted as a function of predicted steady-state droplet temperature. Results presented in Table 3 and Fig. 8 indicate a deviation of 0.1–9% in HOV prediction and 3–21% in vapor pressure prediction. Reference data are overlaid on the plots for direct comparison with the predicted data. As observed in the figure, HOV is relatively insensitive to temperature. Vapor pressure on the other hand, shows higher sensitivity and increases with temperature. Figure 8 also shows a higher HOV for isobutanol, which is also consistent with its lower vapor pressure, given its lower volatility. Predicted results for *n*-heptane and PRF 84 closely follow each other consistent with the similar evaporation rate for both fuels as presented in Fig. 6.

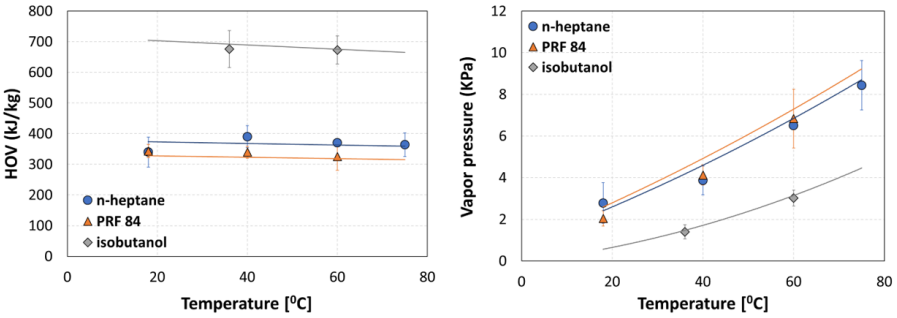

Fig. 8 HOV and vapor pressure predictions as a function of ambient air temperature for the three fuels tested in this work.

Figure 9 shows bar charts comparing predictions for HOV at 25°C and RVP of the three fuels tested in this work. HOV is obtained by interpolating data shown in Fig. 8. RVP is assumed to be the same as fuel vapor pressure evaluated at a droplet temperature of 37.8°C (100°F). However, the ambient air temperature that corresponds to this droplet temperature is close to 95°C for *n*-heptane and PRF 84, which is outside of the measurement range as shown in

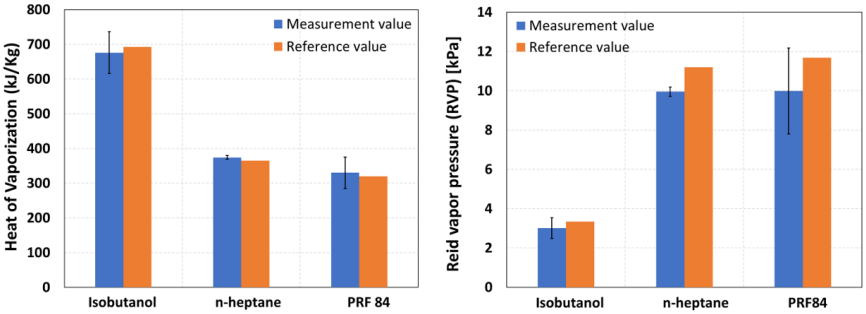

Fig. 9 Measurement results compared with reference data for HOV at 25°C and RVP estimated at 37.8°C. Both temperatures refer to the fuel temperature.

Fig. 8. The vapor pressure at 37.8°C is evaluated using the Clausius-Clapeyron equation (Eq. (11)). The deviation in HOV for predictions as compared to reference values is observed to be in the range of 2–3%. However, for RVP, higher deviations are observed in the range of 10–15%. While the source for the deviations is likely the error in droplet evaporation rate measurement, the results also signify the sensitivity of vapor pressure to HOV through the use of the Clausius-Clapeyron equation. As seen from Eq. 11, small errors in HOV and droplet temperature can lead to large error in vapor pressure due to the exponential nature of the relationship. This is also illustrated by the results in Fig. 10 where the % error induced in vapor pressure calculations is correlated to % error incurred in HOV calculations.

4.3 Physical property predictions using Scheme II

Section 4.2 discussed the use of Scheme I as summarized in Table 1 to estimate HOV and vapor pressure given measurements of droplet size change as a function of time during the evaporation process. Currently there are no diagnostics for droplet temperature measurement. This precludes the use of Scheme-II with complementary experiments to improve upon the number and quality of predicted fuel properties as summarized in Table 1. In the absence of experimental data to facilitate this more advanced scheme, numerical tests are carried

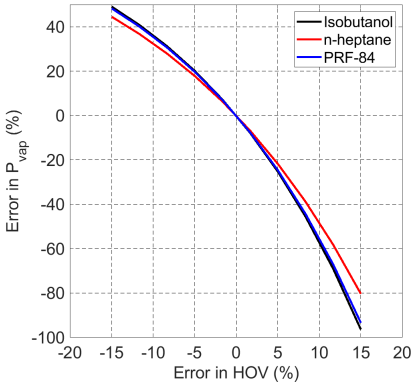

Fig. 10 Error induced in vapor pressure prediction as a function of error incurred in HOV calculations.

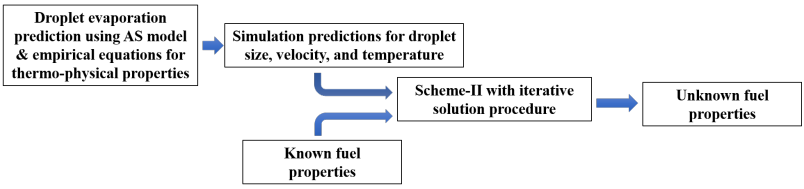

Fig. 11 Fuel property prediction approach using Scheme-II.

out to illustrate the viability of this scheme to predict unknown fuel properties. Figure 11 shows the calculation procedure. The Abramzon-Sirignano (AS) model is used to predict droplet size, velocity, and temperature during the evaporation process using as input, physical properties obtained from reference data sources in the form of empirical equations. Such relationships were obtained for HOV [35], vapor pressure [29], and diffusion coefficient [11]. Data from these simulations are then used as inputs along with unknown properties as summarized in Table 1 to perform calculations based on Scheme II as described in Appendix A. The Scheme employs a solution of Clausius-Clapeyron and Antoine's equations based on evaporation simulation results, to predict unknown physical properties.

Scheme-II uses droplet temperature measurement, which is otherwise obtained from the steady-state energy balance equation (Eq.13). This obviates the need to know the vapor specific heat as an input quantity. Further, having the droplet temperature measurement allows for use of the Antoine equation (after estimation of Antoine constants by data-fitting) to find the boiling point of the fuel. Using the Antoine equation, a differential form of the Clausius-Clapeyron equation can be employed to solve for HOV, which can reduce the prediction error as compared to Scheme-I. This also allows for accurate prediction of both the LJ parameters (σ and ϵ/k). Results for fuel physical properties obtained from Scheme-II are compared with reference data. Results from the evaporation model, used as inputs for Scheme-II as illustrated in Fig. 11 inherently incorporate model assumptions (Section 2), which can be violated by non-ideal conditions in the actual experiment. Thus the fuel property predictions reported through Scheme-II represent a best-case scenario. Exact validation of the Scheme will require measurements at the specific test conditions incorporating droplet velocity and temperature measurements.

Calculations are carried out for evaporation of n-heptane droplets at atmospheric pressure while varying the ambient air temperature. All tests use an initial droplet diameter of 36 μm, with an initial velocity of 0.8 m/s. These values are consistent with results that are obtained using tests with the current droplet generator device. Scheme-II expands upon Scheme-I to predict diffusion coefficients and the Lennard-Jones (LJ) potential parameters (σ and ϵ). Diffusion coefficient represents temperature and pressure dependent binary mass diffusion coefficients, which can be used to compute evaporation mass flux along with a concentration gradient. LJ parameters help define the LJ interaction between molecules through the intermolecular potential function [19]. The species-specific LJ parameters are extensively used in determination of

Case	Fuel	Carrier gas	Inputs			Outputs		
			Initial droplet size	Initial droplet velocity	Carrier gas temperature	Droplet temperature	Evaporation rate	Velocity Decay rate
A	*n*-heptane	Air	36	0.8	313.15	292.53	1.59E-8	0.354
B					333.15	300.07	2.51E-8	0.584
C					343.15	303.11	3.06E-8	0.771
D					353.15	305.77	3.60E-8	0.997
E					373.15	310.19	4.71E-8	1.188
F					393.15	313.64	5.85E-8	1.441
			μm	m/s	K	K	m^2/s	m/s^2

Table 4 Test conditions for Scheme II.

Case	HOV			Vapor pressure			Diffusion coefficient			Lennard-Jones parameters		
	Predicted	Reference	Deviation	Predicted	Reference	Deviation	Predicted	Reference	Deviation	Predicted	Reference	Deviation
A	367	366	0.34	4.60	4.64	0.98	7.13E-6	7E-6	2.16	σ		
B	363	364	0.41	6.89	6.89	0.09	7.63E-6	7.57E-6	0.83	6.25	6.74	7.7
C	361	363	0.73	8.08	8.08	0.01	7.87E-6	7.82E-6	0.64	$\AA$		%
D	359	3625	1.03	9.28	9.29	0.17	8.11E-6	8.04E-6	0.77	ϵ/k		
E	356	362	1.57	11.63	11.67	0.37	8.55E-6	8.48E-6	0.86	459.6	425	8.1
F	353	360	2.03	13.89	13.91	0.12	8.98E-6	8.93E-6	0.56	K		%
	kJ/kg		%	kPa		%	m^2/s		%			

Table 5 Results from calculations using Scheme II.

transport properties as transport processes are driven by momentum exchange between particles [38, 18]. Table 4 summarizes the test conditions used for Scheme II, which are categorized as cases from A–F, with varying ambient air temperature. Table 4 also shows outputs from the evaporation model, which are then used with known fuel properties, in Scheme-II to obtain unknown fuel property predictions as shown in Fig. 11. Droplet temperature, evaporation rate, and velocity decay rate are all reported at the steady-state condition, defined as when the droplet temperature reaches equilibrium and net heat transfer into the droplet is approximately zero. The increase in velocity decay rate observed in Table 4 is due to an increase in drag coefficient resulting from a decreasing Reynolds number associated with a faster evaporation rate.

Calculations for Scheme II are pursued with the initial conditions described in Table 4 using the algorithm detailed in Appendix B.1. Table 5 summarizes the results obtained from the calculations. Table 5 shows temperature-dependent predictions for HOV, vapor pressure, diffusion coefficient, and LJ parameters (σ and ϵ/k), along with reference values and prediction error percentage. As can be observed, HOV and vapor pressure predictions, using Scheme-II, show considerable improvement as compared to Scheme-I results in Table 3. Deviations in predictions are observed to be 0.3–2% for HOV and 0.01–1% for vapor pressure. Diffusion coefficients are predicted within 0.6–2% and deviations in LJ parameter predictions are within 8% for both σ and ϵ/k. The improvement in Scheme-II predictions primarily arise from the ability to use droplet temperature data as obtained from the simulations to evaluate coefficients in the Antoine's equation and subsequently use the differential form of the Clausius-Clapeyron equation to predict HOV resulting in lower deviations from the reference value.

5 Conclusions

The need for small-volume, high-throughput, physical property screening techniques for evaluation of bio-blendstocks with potential to be used as blending components with conventional fuels has motivated the development of droplet evaporation-based property measurement techniques. Evaporation measurements of single droplets at controlled ambient conditions is used in conjunction with transient, zero-dimensional droplet evaporation models and input values for known physical properties to determine unknown properties. This includes temperature dependent heat of vaporization and vapor pressure. Using the Abramzon-Sirignano droplet evaporation model, two different schemes are proposed, which utilize progressively increasing number of input measurements to generate correspondingly higher number of property predictions. The baseline Scheme-I requires the droplet evaporation rate, while Scheme-II additionally requires droplet velocity and droplet temperature. Scheme-II provides predictions for diffusion coefficients and Lennard-Jones potential parameters, σ and ϵ/k in addition to heat of vaporization and vapor pressure.

A droplet generator-based setup implemented in a temperature-controlled chamber is used with high-resolution imaging to measure droplet evaporation rates for various liquid fuels including *n*-heptane, isobutanol, and PRF 84 which is a blend of 84% *iso*-octane with 16% *n*-heptane. Evaporation rates are used with the Scheme-I algorithm to predict temperature-dependent HOV and vapor pressure for all three fuels. Deviations of 0.1–9% and 3–21% are observed for predictions of HOV and vapor pressure respectively as compared to reference data from literature. Deviations for both properties are found to decrease with increasing temperature owing to reduced error in measured droplet evaporation rate given the larger size change, as well as improvements in the prediction algorithm performance. The use of the Clausius-Clapeyron

equation is found to make error in vapor pressure predictions highly sensitive to error in HOV calculations. Temperature-dependent HOV and vapor pressure predictions are interpolated to find HOV at 25°C and the Reid vapor pressure (estimated as vapor pressure at 37.8°C). Predictions show an overall deviation of 2–3% for HOV and 10–15% for RVP.

Lacking droplet temperature measurements, Scheme-II is evaluated numerically by using input values generated by droplet evaporation models to carry out the algorithms and make physical property predictions. The availability of droplet velocity and temperature for Scheme II, along with elimination of experimental droplet evaporation rate errors, and use of the Clausius-Clapeyron equation in a differential form is found to have a strong influence on error in property predictions. Deviations in property predictions are reduced, with Scheme II calculations predicting HOV and vapor pressure with deviations of 0.3–2% and 0.01–1% respectively. Further, diffusion coefficients and LJ parameters are predicted within 5% and 8% respectively.

Overall, the proposed algorithms in conjunction with experimental measurements show the viability of using droplet-evaporation based techniques for small-volume $\mathcal{O}(\mu l)$, high-throughput $\mathcal{O}(ms)$ screening tools for down selection of liquid fuels on the basis of physical properties relevant to in-cylinder engine processes. Performance of current schemes can be considerably improved by reducing droplet evaporation rate errors through use of larger droplets as well as higher-resolution imaging techniques. Finally, Scheme-II has the potential to reduce the number of inputs required for property prediction as well as increase the number and accuracy of predictions. Scheme-II, which has been numerically validated in the present work will be evaluated using experimental techniques in future work by incorporating diagnostics for droplet velocity and temperature measurements.

Acknowledgments. This research was conducted as part of the Co-Optimization of Fuels & Engines (Co-Optima) project sponsored by the U.S. Department of Energy (DOE) Office of Energy Efficiency and Renewable Energy (EERE), Bioenergy Technologies and Vehicle Technologies Offices.

Appendix A Property definition

$$Sh^* = 2 + \frac{(Sh_0 - 2)}{F_M}; \quad Nu^* = 2 + \frac{(Nu_0 - 2)}{F_T} \tag{A1}$$

$$Sh_0 = 1 + (1 + ReSc)^{1/3}\phi\,(Re)\,; \quad Nu_0 = 1 + (1 + RePr)^{1/3}\phi\,(Re) \tag{A2}$$

$$F_{(T,M)} = (1 + B_{(T,M)})^{0.7}\frac{\ln\left(1 + B_{(T,M)}\right)}{B_{(T,M)}} \tag{A3}$$

where $\phi\,(Re) = 1$ for $Re \leq 1$ and $\phi\,(Re) = Re^{0.077}$ when $1 < Re \leq 400$

The fuel vapor mass fraction of the film and its temperature are evaluated based on '1/3 rule' recommended in the work of Yuen and Chen [36] given by,

$$\bar{T}_f = T_i + \frac{(T_\infty - T_i)}{3}; \quad \bar{Y}_F = Y_i + \frac{(Y_\infty - Y_i)}{3} \tag{A4}$$

For the simulations, which provide input to Scheme-II, the empirical diffusion coefficient Eqn.A5 defined in the work of Fuller et. al [11] was employed.

$$\bar{\chi}_{fc} = \frac{0.00143\bar{T}_f^{1.75} \times 10^{-4}}{P_\infty M_{fc}^{0.5}\left(\zeta_c^{1/3} + \zeta_f^{1/3}\right)^2} \tag{A5}$$

where ζ is the diffusion volume, evaluated based on sum of element wise contributions. For the present study, the diffusion volume for air $\zeta_c = 19.7$ and diffusion volume of *n*-heptane vapor, $\zeta_f = 148.2$.

Similarly, the temperature dependent HOV of *n*-heptane is defined based on the handbook of Yaws [35], given by

$$H_F = (A_v(1 - T_i/T_c)^{n_v}) \times 10^6/MW_F; \tag{A6}$$

where, for n-heptane, $A_v = 49.73, T_c = 540.26,$ & $n_v = 0.360$. The temperature dependent vapor pressure is evaluated by Antoine equation given by,

$$\log_{10}(P_{vap}) = A - \frac{B}{(C + T_i - 273)} \tag{A7}$$

where, for n-heptane, $A = 4.0404, B = 1263.909, C = 216.432$.

The vapor phase thermal conductivity was defined based on the work of Chung et. al [29], expressed as,

$$k_F = \frac{\mu_F 3.75 \psi R_u}{MW_F} \tag{A8}$$

$$\psi = 1 + \alpha \left[\frac{(0.215 + 0.28288\alpha - 1.061\beta + 0.2665Z)}{(0.6366 + \beta Z + 1.061\alpha\beta)} \right] \tag{A9}$$

where $\alpha = \frac{C_v}{R} - 1.5$, $\beta = 0.7862 - 0.7109\omega + 1.3618\omega^2$ and $Z = 2.0 + 10.5\frac{T_f}{T_c}$. T_c represents the critical temperature of the fuel and ω refers to the accentric factor of the fuel. For fuel vapor specific heat and viscosity, fourth order and third order polynomials of temperature are respectively employed, with the material specific polynomial coefficients listed in the work of Poling et. al [29] and Yaws et. al [35]

Appendix B Algorithm for Scheme-II

The pertinent steps of the Scheme-II algorithm are listed below:

1. Using the droplet temperature, experimental data and property inputs as listed in Table. 1, the governing equation for droplet velocity is utilized to solve for interface fuel vapor mass fraction Y_{Fi}. Accordingly, Eq. 3 is interpreted as an implicit function of Y_{Fi} and T_i, as shown below:

$$\frac{du}{dt} + \frac{3C_D\bar{\rho}_f}{8D_l\rho_l}(u-u_\infty)^2 - g_0\left(1-\frac{\bar{\rho_f}}{\rho_l}\right) = E(Y_{Fi}, T_i) = 0 \tag{B10}$$

The above equation can be solved for unknown interface mass fraction Y_{Fi}, using any standard root finding technique.

2. The interface mass fraction (Y_{Fi}) is utilized to find the instantaneous vapor pressure of the droplet, which is defined as

$$P_{vap} = P_\infty \left\{ \frac{Y_{Fi}MW_c}{MW_F + Y_{Fi}(MW_c - MW_F)} \right\} \tag{B11}$$

where MW is the molecular weight of carrier gas (subscript 'c') and fuel (subscript 'F').

3. Using the interface mass fraction and temperature, the mass balance equation Eq. 6 is solved for the unknown film diffusion coefficient $\bar{\chi}_{fc}$, which is expressed as:

$$\bar{\chi}_{fc} = \frac{\dot{m}}{\pi\bar{\rho}_f D_l \mathrm{Sh}^* ln(1+B_M)} \tag{B12}$$

4. The above steps are repeated for experiments with different carrier gas temperature. The resulting equilibrium droplet temperature for each experiment and vapor pressure, evaluated from the Step.2 , are employed to find the Antoine constants $(A, B, \ \&C)$ for the tested liquid, by fitting Antoine equation to the experimental data, expressed as,

$$\log_{10}(P_{vap}) = A - \frac{B}{(C+T_i-273)} \tag{B13}$$

5. Using the Antoine constants in Antoine equation Eq. B13, the boiling point (T_{boil}) of the tested liquid can be determined. Also, HOV can be determined by using the differential form of Clausius Clapeyron equation, given by

Eqn. B14, instead of Eqn. 11, which can improve the accuracy of HOV predictions.

$$\frac{dP_{vap}}{dT} = \frac{P_{vap} H_F}{T^2 R_v} \tag{B14}$$

6. The predicted diffusion coefficients, for each experiment, is used to evaluate the Lennard Jones parameters, using the following empirical definition for diffusion coefficient, based on the work of Wilke and Lee [33].

$$\bar{\chi}_{fc} = \frac{[3.03 - (0.98/MW_{fc}^{0.5})](10^{-7})\bar{T}_f^{3/2}}{P_\infty (MW_{fc}^{0.5})\sigma_{fc}^2 \Omega_D} \tag{B15}$$

where,

$$MW_{fc} = 2\left[\frac{1}{MW_F} + \frac{1}{MW_c}\right]^{-1}$$
$$\sigma_{fc} = \frac{(\sigma_c + \sigma_F)}{2}$$

The subscript 'c' represents the carrier gas and 'F' represents the fuel vapor. Ω_d represents the collision integral, in terms of Lennard Jones parameters (σ, ϵ), given by:

$$\Omega_d = \frac{A}{(T^*)^B} + \frac{C}{\exp(DT^*)} + \frac{E}{\exp(FT^*)} + \frac{G}{\exp(HT^*)} \tag{B16}$$

where,

$$T^* = k_b T/\epsilon_{fc} \qquad A = 1.06036 \qquad B = 0.15610$$
$$C = 0.19300 \qquad D = 0.47635 \qquad E = 1.03587$$
$$F = 1.52996 \qquad G = 1.76474 \qquad H = 3.89411$$

$$\epsilon_{fc} = (\epsilon_c \epsilon_f)^{0.5}$$

The two Lennard Jones potential (σ, ϵ) parameters are evaluated by non-linear fitting of Eq. B15 on the diffusion coefficient predictions obtained from Step. 5 of the current algorithm. Using the Boiling point T_{boil} evaluated in Step.5 of the present algorithm, based on the work of Wilke and Lee [33], one of the Lennard Jones Parameter can be defined as $\frac{\epsilon}{k_b} = 1.15 T_{boil}$. Using this definition for $\frac{\epsilon}{k_b}$, the diffusion coefficient equation Eq. B15 can be used only to evaluate one of the Lennard Jones Potential (σ), which is observed to improve the prediction accuracy.

References

[1] Abramzon B, Sirignano W (1989) Droplet vaporization model for spray combustion calculations. International journal of heat and mass transfer 32(9):1605–1618

[2] Aggarwal S, Peng F (1995) A review of droplet dynamics and vaporization modeling for engineering calculations. Journal of Engineering for Gas Turbines and Power 117(3):453–461

[3] Bhatia SK, Kim SH, Yoon JJ, et al (2017) Current status and strategies for second generation biofuel production using microbial systems. Energy Conversion and Management 148:1142–1156

[4] Chow EW, Heywood JB, Speth RL (2014) Benefits of a higher octane standard gasoline for the us light-duty vehicle fleet. SAE Technical Paper

[5] Chupka GM, Christensen E, Fouts L, et al (2015) Heat of vaporization measurements for ethanol blends up to 50 volume percent in several hydrocarbon blendstocks and implications for knock in si engines. SAE International Journal of Fuels and Lubricants 8(2):251–263

[6] Dang W, Zhao W, Schoegl I, et al (2020) A small-volume, high-throughput approach for surface tension and viscosity measurements of liquid fuels. Measurement Science and Technology 31(9)

[7] Dang W, Gurunadhan M, Schoegl I, et al (2021) Temperature effects on droplet oscillation decay with application to fuel property measurement. Atomization and Sprays 31(10)

[8] Fioroni GM, Fouts L, Christensen E, et al (2018) Measurement of heat of vaporization for research gasolines and ethanol blends by dsc/tga. Energy & Fuels 32(12):12,607–12,616

[9] Fioroni GM, Christensen ED, Fouts LA, et al (2019) Heat of vaporization and species evolution suring gasoline evaporation measured by dsc/t-ga/ms for blends of c1 to c4 alcohols in commercial gasoline blendstocks. Tech. rep., National Renewable Energy Lab.(NREL), Golden, CO (United States)

[10] Foucher F, Higelin P, Mounaim-Rousselle C, et al (2013) Influence of ozone on the combustion of n-heptane in a hcci engine. Proceedings of the Combustion Institute 34(2):3005–3012

[11] Fuller EN, Schettler PD, Giddings JC (1966) New method for prediction of binary gas-phase diffusion coefficients. Industrial & Engineering Chemistry 58(5):18–27

[12] Gaspar DJ, Phillips SD, Polikarpov E, et al (2019) Measuring and predicting the vapor pressure of gasoline containing oxygenates. Fuel 243:630–644

[13] Gaspar DJ, West BH, Ruddy D, et al (2019) Top ten blendstocks derived from biomass for turbocharged spark ignition engines: Bio-blendstocks with potential for highest engine efficiency. Tech. rep., Pacific Northwest National Lab.(PNNL), Richland, WA (United States)

[14] Hatzioannidis I, Voutsas EC, Lois E, et al (1998) Measurement and prediction of reid vapor pressure of gasoline in the presence of additives. Journal of Chemical & Engineering Data 43(3):386–392

[15] Isfahani SNR, Sauer VM, Schoegl I (2021) Effects of dilution and pressure on combustion characteristics within externally heated micro-tubes. Proceedings of the Combustion Institute 38(4):6695–6702

[16] Kalghatgi GT (2001) Fuel anti-knock quality-part i. engine studies. SAE Transactions pp 1993–2004

[17] Kar K, Last T, Haywood C, et al (2009) Measurement of vapor pressures and enthalpies of vaporization of gasoline and ethanol blends and their effects on mixture preparation in an si engine. SAE International Journal of Fuels and Lubricants 1(1):132–144

[18] Kee RJ, Dixon-Lewis G, Warnatz J, et al (1986) A fortran computer code package for the evaluation of gas-phase multicomponent transport properties. Sandia National Laboratories Report SAND86-8246 13:80,401–1887

[19] Kee RJ, Coltrin ME, Glarborg P (2005) Chemically reacting flow: theory and practice. John Wiley & Sons

[20] Landera A, Mac Dowell N, George A (2021) Development of robust models for the prediction of reid vapor pressure (rvp) in fuel blends and their application to oxygenated biofuels using the saft-γ approach. Fuel 283:118,624

[21] McCormick RL, Fioroni G, Fouts L, et al (2017) Selection criteria and screening of potential biomass-derived streams as fuel blendstocks for advanced spark-ignition engines. SAE International Journal of Fuels and Lubricants 10(2):442–460

[22] Mendes G, Aleme HG, Barbeira PJ (2017) Reid vapor pressure prediction of automotive gasoline using distillation curves and multivariate calibration. Fuel 187:167–172

[23] Obergruber M, Honig V, Prochazka P, et al (2021) Physicochemical properties of biobutanol as an advanced biofuel. Materials 14(4):914

[24] Putnam A (1961) Integratable form of droplet drag coefficient. Ars Journal 31(10):1467–1468

[25] Qian Y, Wang X, Zhu L, et al (2015) Experimental studies on combustion and emissions of rcci (reactivity controlled compression ignition) with gasoline/n-heptane and ethanol/n-heptane as fuels. Energy 88:584–594

[26] Ratcliff MA, Burton JL, Sindler P, et al (2018) Effects of heat of vaporization and octane sensitivity on knock-limited spark ignition engine performance. Tech. rep., National Renewable Energy Lab.(NREL), Golden, CO (United States)

[27] Ratcliff MA, Windom B, Fioroni GM, et al (2019) Impact of ethanol blending into gasoline on aromatic compound evaporation and particle emissions from a gasoline direct injection engine. Applied Energy 250:1618–1631

[28] Ray AK, Davis EJ, Ravindran P (1979) Determination of ultra-low vapor pressures by submicron droplet evaporation. The journal of chemical physics 71(2):582–587

[29] Reid RC, Prausnitz JM, Poling BE (1987) The properties of gases and liquids. McGraw Hill Book Co., New York, NY

[30] Sarathy SM, Kukkadapu G, Mehl M, et al (2015) Ignition of alkane-rich face gasoline fuels and their surrogate mixtures. Proceedings of the Combustion Institute 35(1):249–257

[31] Sazhin SS (2006) Advanced models of fuel droplet heating and evaporation. Progress in energy and combustion science 32(2):162–214

[32] Splitter DA, Szybist JP (2014) Experimental investigation of spark-ignited combustion with high-octane biofuels and egr. 2. fuel and egr effects on knock-limited load and speed. Energy & Fuels 28(2):1432–1445

[33] Wilke C, Lee C (1955) Estimation of diffusion coefficients for gases and vapors. Industrial & Engineering Chemistry 47(6):1253–1257

[34] Wyszynski LP, Stone CR, Kalghatgi GT (2002) The volumetric efficiency of direct and port injection gasoline engines with different fuels. Tech. rep., SAE Technical Paper

[35] Yaws CL (2008) Thermophysical properties of chemicals and hydrocarbons. William Andrew

[36] Yuen M, Chen L (1976) On drag of evaporating liquid droplets. Combustion Science and Technology 14:147–154

[37] Zeng W, Xu M, Zhang M, et al (2012) Macroscopic characteristics for direct-injection multi-hole sprays using dimensionless analysis. Experimental thermal and fluid science 40:81–92

[38] Zheng C, Coombs DM, Akih-Kumgeh B (2019) Real gas model parameters for high-density combustion from chemical kinetic model data. ACS omega 4(2):3074–3082